

Be–B thin film growth: A deep potential and molecular dynamics study

Xilei Wang(王熙蕾) and Hong Zhang(张红)

Citation: Chin. Phys. B, 2026, 35 (**4**): 046801. DOI: 10.1088/1674-1056/ae0309
http://cpb.iphy.ac.cn; http://iopscience.iop.org/cpb

What follows is a list of articles you may be interested in

Reconstruction and stability of Fe_3O_4(001) surface: An investigation based on particle swarm optimization and machine learning

Hongsheng Liu(柳洪盛), Yuanyuan Zhao(赵圆圆), Shi Qiu(邱实), Jijun Zhao(赵纪军), and Junfeng Gao(高峻峰)
Chin. Phys. B, 2023, 32 (**5**): 056802. DOI: 10.1088/1674-1056/acb9e4

Atomistic insights into early stage corrosion of bcc Fe surfaces in oxygen dissolved liquid lead-bismuth eutectic (LBE-O)

Ting Zhou(周婷), Xing Gao(高星), Zhiwei Ma(马志伟), Hailong Chang(常海龙), Tielong Shen(申铁龙), Minghuan Cui(崔明焕), and Zhiguang Wang(王志光)
Chin. Phys. B, 2023, 32 (**3**): 036801. DOI: 10.1088/1674-1056/ac834b

Effect of an electric field on dewetting transition of nitrogen-water system

Qi Feng(冯琦), Jiaxian Li(厉嘉贤), Xiaoyan Zhou(周晓艳), and Hangjun Lu(陆杭军)
Chin. Phys. B, 2022, 31 (**3**): 036801. DOI: 10.1088/1674-1056/ac1e21

Oxidation degree dependent adsorption of ssDNA onto graphene-based surface

Huishu Ma(马慧姝), Jige Chen(陈济舸), Haiping Fang(方海平), and Xiaoling Lei(雷晓玲)
Chin. Phys. B, 2021, 30 (**10**): 106806. DOI: 10.1088/1674-1056/abf109

Tolman length of simple droplet: Theoretical study and molecular dynamics simulation

Shu-Wen Cui(崔树稳), Jiu-An Wei(魏久安), Qiang Li(李强), Wei-Wei Liu(刘伟伟), Ping Qian(钱萍), and Xiao Song Wang(王小松)
Chin. Phys. B, 2021, 30 (**1**): 016801. DOI: 10.1088/1674-1056/abb65a

---

Be–B thin film growth: A deep potential and molecular dynamics study

Xilei Wang(王熙蕾)[1] and Hong Zhang(张红)[1,2,†]

[1] *College of Physics, Sichuan University, Chengdu* 610065, *China*

[2] *Key Laboratory of High Energy Density Physics and Technology of Ministry of Education, Sichuan University, Chengdu* 610065, *China*

(Received 24 April 2025; revised manuscript received 29 July 2025; accepted manuscript online 4 September 2025)

Beryllium–boron (BeB) thin films are important target materials in inertial confinement fusion (ICF) experiments. In this work, molecular dynamics simulations combined with deep learning methods were employed to investigate the deposition behavior and structural evolution of BeB films. The effects of incident angle, incident energy and substrate temperature on the film growth process were systematically studied. A deep learning approach was used to develop interaction potentials based on Be and B elements and the known BeB crystalline phases, enabling an accurate description of cluster growth during deposition. The simulation results indicate that appropriate control of the incident parameters and substrate temperature can significantly improve the surface quality of the films. These findings may offer preliminary insights into the optimization of experimental conditions for the fabrication of high-quality BeB thin films.

Keywords: growth of beryllium–boron films, deep potential energy function, molecular dynamics simulation, cluster sputtering

PACS: 68.55.–a, 81.15.Aa

DOI: 10.1088/1674-1056/ae0309 **CSTR:** 32038.14.CPB.ae0309

1. Introduction

A proper and high-quality target material is one of the key factors in inertial confinement fusion (ICF) experiments.[1–3] Due to its low density (1.85 times that of water), low x-ray reflectivity, high melting point and high flexural rigidity,[4] beryllium (Be) metal is a suitable ablator material in the field of ICF.[5–7] Magnetron sputtering is the primary method used in experiments to prepare target pellets.[8] During the fabrication of Be targets, Be atoms grow in a hexagonal close packed (hcp) structure along the substrate crystal, forming a columnar structure. The rough columnar grains can weaken the mechanical properties of the coating, making it prone to damage from external conditions. The anisotropic characteristics of the grains also cause the coating to exhibit different properties in different directions, reducing overall stability and affecting the ablation performance of the material.[9]

To address the issue of surface roughness in Be targets, researchers have proposed several grain refinement techniques, including a negative bias voltage on the substrate,[10] ion bombardment[11] and doping with impurities such as boron (B).[12] Studies have shown that doping Be with B atoms during the growth process can promote uniform grain refinement, reduce surface roughness and even form an amorphous glass-like structure.[12–14] Jankowski *et al.*[12] revealed that B doping can effectively refine the columnar structure to less than 20 nm in width, significantly reducing the surface roughness of thin films. Li *et al.*[13] showed that as the proportion of B doping increased to around 10% to 12%, the structure of BeB films transitioned from crystalline to amorphous, with a notable weakening of columnar crystal growth. Xu *et al.*[14] used magnetron sputtering to prepare BeB amorphous films and found that films grown with a B content of 11%–12% exhibit an amorphous, uniform and smooth structure, which reduces the effects of Rayleigh–Taylor instabilities.

To achieve high-quality BeB target pellets, it is essential to precisely control and thoroughly investigate key parameters in the magnetron sputtering process.[8] However, due to the limitations of experimental scales it is difficult to explore the microscopic mechanisms and morphological evolution of the growth of BeB films in detail. Moreover, the potential toxicity of Be further constrains experimental studies.[15] Molecular dynamics (MD) simulations offer a way to investigate the growth of films at an atomic scale.[16,17] In magnetron sputtering experiments, atoms bombarded from the target material have a certain probability of arriving at the substrate as clusters. Considering the significant impact of incident clusters on the process of growth, it is essential to study the deposition of BeB atoms in clusters on the substrate. In fact, the properties of Be clusters and the deposition of atoms in clusters have been reported as one of the key factors affecting the microstructure and performance of thin films.[18–21] Apart from the influence of clusters on the growth of films, several factors such as incident angle,[22] incident energy[23] and substrate temperature[24] are also important. Numerous MD sim-

†Corresponding author. E-mail: hongzhang@scu.edu.cn

© 2026 Chinese Physical Society and IOP Publishing Ltd. All rights, including for text and data mining, AI training, and similar technologies, are reserved.

ulations of the growth of films have been reported,[25–32] focusing on the dynamic processes and structural characteristics of thin films, particularly the influence of incident conditions on the structure and morphology of deposited films. Zhou *et al.*[25–27] used MD simulations to analyze the effects of incident angle, atomic kinetic energy and substrate temperature on morphology and microstructure. Mes-adi *et al.*[28] investigated the growth of aluminum films on different termination surfaces (Al-terminated and Ni-terminated) using NiAl alloys as substrates. Byggmästar *et al.*[29] simulated the growth of films on a Be substrate, observing the early stages of oxide layer formation on the Be surface and predicting the thermodynamic and elastic properties of BeO nanosheets. Brault *et al.*[30] utilized the ReaxFF force field for MD simulations to study the growth of palladium (Pd) and palladium oxide (PdO) nanoclusters, highlighting the influence of nanocluster temperature on the simulated growth process. Zhu *et al.*[31] studied the growth characteristics of copper films on silicon substrates at different temperatures, and found that the proportion of face-centered cubic (fcc) structure rose with increasing temperature in the deposited films. In addition, interface mixing was primarily dominated by diffusion of copper atoms, while the impact of incident sputtered atoms led to densification at the film–substrate interface. Sharkass *et al.*[32] explored the response of an oxidized tungsten surface to deuterium irradiation in the 5–120 eV impact energy range and analyzed the retention, reflection, sputtering and surface chemistry of oxidized layers at various thicknesses at room temperature. Although MD methods have been widely applied in the simulation of film growth, simulation studies on magnetron sputtering growth of BeB films are rare.

In MD simulations, the potential function describes the interactions between particles in the system. The position and velocity of each particle are governed by Newton's laws of motion. The potential function provides the driving force for these movements; however, due to the lack of a comprehensive potential function for Be and B, researchers often adopt a hybrid approach by calculating the potentials of Be and B atoms separately. For instance, the embedded atom method (EAM) is used for pure Be[33] and the Tersoff potential is applied for pure B.[34] This method is not sufficient to accurately describe complex deposition behaviors. Additionally, mixing different types of potential functions carries the risk of force mismatches at the boundary atoms. Therefore, it is crucial to develop a multibody potential function that can handle high doping concentrations and encompass the multiphase structure of BeB systems.

Machine learning interatomic potentials (MLIPs) have emerged as efficient alternatives to classical potentials, offering near-*ab initio* MD (AIMD) accuracy with a much lower computational cost. Unlike empirical models, MLIPs are trained on quantum data and lack explicit physical expressions. These include the Gaussian approximation potential,[35] deep potential (DP),[36] spectral neighbor analysis potential[37] and moment tensor potential.[38] Each potential offers unique advantages and can be tailored for specific types of material science investigations. The DP energy function, a product of deep learning, can construct potential energy descriptions that are applicable to systems with different temperatures and multiple components through intelligent learning by deep neural networks.[36,39] There have been many studies utilizing deep learning to develop DP energy functions and applying them to MD simulations.[40–42] Konashi *et al.*[40] employed a neural network potential for MD simulation of uranium dioxide, which is widely applicable to the evaluation of physical properties. Kim *et al.*[41] developed a machine-learning interatomic potential and calculated diffusion coefficients of Ag in $ZrC_{0.94}$ and $ZrC_{0.97}$ in the temperature range of 2800–3200 K. Liyanage *et al.*[42] created a neural network potential for hydrogen (H) and zirconium (Zr) based on DFT calculations. The DP energy function not only captures energy values with high precision but also ensures accurate force calculations, making it appropriate for describing and simulating force fields in complex systems. Therefore, it is particularly suitable for simulating the growth of large-scale, multi-atomic BeB films.

In this study, we explored various factors influencing the growth of BeB films in magnetron sputtering. To closely align with experimental conditions, we simulated the deposition of Be and B atoms in cluster form. Through detailed simulation analysis, we revealed how factors such as incident angle, incident energy and substrate temperature affect the growth morphology and microstructure of the films during sputtering. These findings provide theoretical support for the design and optimization of BeB target pellet experiments, aiming to enhance the controllability and efficiency of film preparation.

2. Computational method

2.1. The substrate setting

The substrate was constructed by Atomsk software.[43] The substrate is illustrated in Fig. 1. It has a size of 108.47 Å×93.94 Å×121.42 Å, and contains 27648 Be atoms with 2304 atoms per layer. The Be (0001) surface was taken to be perpendicular to the z-axis. The atoms of the substrate were divided into two types: boundary atoms and free atoms. The boundary atoms comprised the bottom four layers of the atoms, with a height of 7.41 Å, which were fixed on their lattice sites to prevent the substrate materials from drifting due to the incident atom momentum transfer. The free atoms consisted of the eight atomic layers above the fixed atoms, where

atoms moved freely according to Newton's laws of motion. This region simulated the free diffusion and collision behavior of deposited atoms. There was a 5 Å space at the top of the simulation box designated as the evaporation layer, which removed any particles that were reflected. The clusters were randomly generated in the region 5 Å to 10 Å above the top surface of the simulation box.

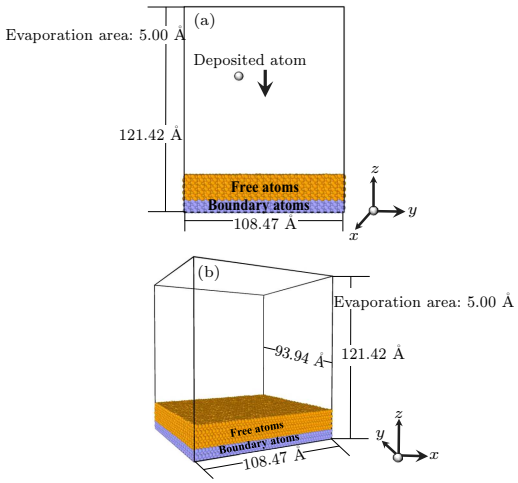


Fig. 1. The simulation model of the substrate: (a) front view, (b) perspective view.

2.2. Details of the MD computational setting

Periodic boundary conditions were applied in the x-axis and y-axis directions. The time step for the MD simulation was 0.002 ps. The temperature was controlled by a canonical ensemble (NVT), with temperature recalibration every 0.2 ps. Before deposition, the substrates were relaxed for 20 ps to ensure that the substrate temperature and structure were in equilibrium. Then, a 300 ps deposition of atoms was carried out to grow the BeB films. The velocities of the deposited atoms were set as

$$v = \sqrt{2E_k/m}, \tag{1}$$

$$v_z = -v\cos\theta, \tag{2}$$

$$v_x = -v\sin\theta\sin\phi, \tag{3}$$

$$v_y = -v\sin\theta\cos\phi, \tag{4}$$

where v is the total velocity of the deposited particles, E_k is the incident energy, m is the mass of the deposited particles, v_x, v_y and v_z are the velocity components of the particles along the x, y and z axes, θ is the angle between the velocity component in the x–y plane and the z-axis and ϕ is the angle between v_x and v_y. The angle θ represents the polar angle between the total velocity and the z-axis, while ϕ denotes the azimuthal angle between velocity projection in the x–y plane and the y-axis.

The interactions between atoms are described by the DP energy function. The Large-scale Atomic/Molecular Massively Parallel Simulator (LAMMPS)[44] with a graphics processing unit[45] was used to simulate the growth of BeB films. The open visualization tool (OVITO)[46] was used to visualize and analyze the simulation results.

The roughness of BeB films was evaluated by surface area. In this study, we primarily used the surface area ratio (SAR) to analyze the roughness of the deposited films. The surface area ratio is defined as

$$\mathrm{SAR} = S_{\mathrm{films}}/S_{\mathrm{substrate}}, \tag{5}$$

where S_{films} is the surface area of the films and $S_{\mathrm{substrate}}$ is the substrate area in the x–y plane. A larger SAR indicates a rougher surface.

The radial distribution function (RDF)[47] was used to describe the spatial distribution probability of two particles in a system. The slope or peak value of this function can reveal the strength of atomic interactions, while the peak position reflects the average distance between atoms. The expression is as follows:

$$g(r) = \frac{1}{\rho 4\pi r^2}\frac{\sum_{t=1}^{T}\sum_{j=1}^{N}\Delta N(r\to r+\delta r)}{N\times t}, \tag{6}$$

where N is the total number of atoms in the system, ρ is the system density, t is the calculation time, δr is the defined distance increment and ΔN is the varying number of atoms.

The mean squared displacement (MSD) is a physical quantity used to describe the average distance traveled by microscopic particles over a certain time interval.[48] In MD simulations, MSD serves as a standard measure of the change in particle positions over a given period. It is defined as the average of the squared displacements of individual particles at each time step. The expression is as follows:

$$\mathrm{MSD}(t) = \frac{1}{N}\sum_{i=1}^{N}\left(r_i(t) - r_i(0)\right)^2, \tag{7}$$

where N is the total number of atoms, $r_i(t)$ is the position of the ith atom at time t, and $r_i(0)$ is its initial position.

2.3. Generating the DP energy function

In this study, the DP energy function was generated by DeepGen.[36] For training amorphous or glass-like structures, a well-suited initial model was considered at different temperatures, which depends on a well-designed neural network. We chose the se_e2_a descriptor (short for DeepPot-SE), which covers the distance and angular information between a specific atom and its neighbors within a cutoff radius, enabling the representation of multibody interactions. The initial data were provided based on AIMD calculations using the Vienna *ab initio* Simulation Package. Furthermore, four neural models with different random seeds were developed which would be compared by LAMMPS.[44] Configurations with high force discrepancies were marked as under-trained, leading to another round of calculations for iterative optimization of the DP model. Further computational details are as follows:

(a) Material selection: we selected representative elemental boron structures (B_{28} *Pnnm*, B_{36} *R*-3*m*) and elemental beryllium (Be_2 *P*63/*mmc*), along with their compounds such as Be_4B (*P*4/*nmm*), Be_8B_4 (*C*2/*m*) and $Be_{12}B_6$ (*P*-62*c*) as the initial systems for model training.

(b) Supercell construction: these structures were expanded into supercells containing approximately 300–500 atoms, with lattice vector lengths exceeding 12 Å to ensure accurate AIMD simulations. The supercells were then uniformly stretched and compressed, with deformation ratios ranging from 0.97 to 1.03.

(c) Atomic and lattice perturbations: to enhance configurational diversity, we applied random perturbations to both atomic positions and lattice vectors of the deformed structures, allowing for the sampling of a wider range of distorted configurations.

(d) AIMD simulations: short AIMD runs were performed under the NVT ensemble at 100 K with a time step of 2 fs for a total of 25 steps in order to avoid generating redundant training data. This procedure yielded atomic snapshots along with relevant quantities such as energy, forces, stress and system size, for BeB structures.

(e) Simulation parameter optimization: the plane-wave energy cutoffs for Be and B were 247 eV and 318 eV, respectively. We used a common cutoff energy of 400 eV, which is sufficient to ensure reliable AIMD results. Given the large size of the supercells, a single Gamma-point *k*-mesh was used for Brillouin zone sampling.

(f) LAMMPS exploration stage: we designed multiple iterations of LAMMPS-based structural exploration using the evolving neural network model. In the first round, we employed the NVT ensemble at target temperatures of 100 K, 200 K and 300 K to sample BeB crystals and their (100), (010) and (001) surface configurations. The second round used the NPT ensemble under ambient pressure to explore bulk BeB compounds and selected surface structures. The third and fourth rounds increased the number of MD steps from 500 to 3000 to expand the configurational space and improve potential coverage. In the fifth and sixth rounds, the temperature was increased to 400 K, 500 K and 600 K to study structural behavior at elevated temperatures.

3. Results

3.1. The reliability of the DP energy function

We conducted a comprehensive analysis of the training results for the loss function, which quantified the difference between the predictions of models and the actual results (DFT calculations), serving as the objective for the optimization algorithm during the training process. In summary, the loss function measured the degree of error in the predictions of models

$$L(p_\epsilon, p_f, p_\xi) = \frac{p_\epsilon}{N}\Delta\epsilon^2 + \frac{p_f}{3N}\sum_i |\Delta F_i|^2 + \frac{p_\xi}{9N}\|\Delta\xi\|^2. \quad (8)$$

This formula presents the contributions of energy, force and virial to the loss function. Since the force was related to the first derivative of energy and the virial was associated with the second derivative of energy, a common practice in characterizing a system is to use energy and force. Therefore, we only consider the roles of energy and force in the loss function moving forward.

Figure 2 shows that as the learning rate decreases from 10^{-3} to 10^{-8}, the total loss function (blue curve) gradually decreases and reaches equilibrium at around 10^6 training steps. The energy loss function (orange curve) stabilizes around 10^{-3}, and the force loss function (green curve) stabilizes around 10^{-1}, indicating that the model has achieved a certain level of stability.

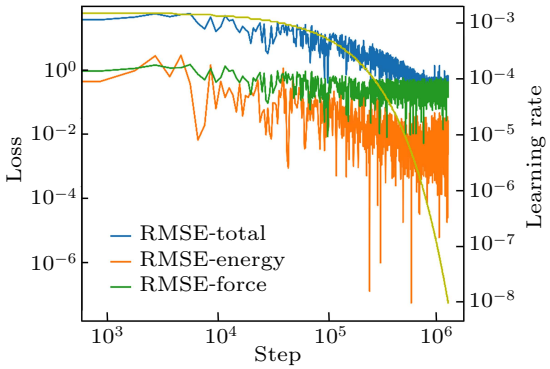


Fig. 2. The variation curves of energy and force loss functions over time (blue, total; orange, energy; green, force).

In addition, fundamental model validation requires sampling calculations from the first-principles dataset to verify specific accuracy across different systems. The fitting results for elemental Be and B and some of their compounds are shown in Figs. 3 and 4. From the scatter and histogram plots in Figs. 3(a), 3(c), 4(a), and 4(c), force prediction errors for the test set are highly concentrated (red dashed circle regions), indicating that most data points fall within a small error range. In detail, Figs. 3(a), 3(c), 4(a), and 4(c) show that the force for Be, B_{36}, Be_8B_4 and Be_4B is primarily below 0.5 eV Å^{-1}, 1.0 eV Å^{-1}, 0.8 eV Å^{-1} and 0.75 eV Å^{-1} with discrepancies between DFT self-consistent calculations and predicted values largely within 0.05 eV Å^{-1}, 0.15 eV Å^{-1}, 0.13 eV Å^{-1} and 0.08 eV Å^{-1}, respectively. The line plots in Figs. 3(b), 3(d), 4(b), and 4(d) offer another perspective on fitting performance: both energy and force predictions show a near-linear relationship with DFT values, indicating that the developed deep potential function has achieved a satisfactory level of performance through training.

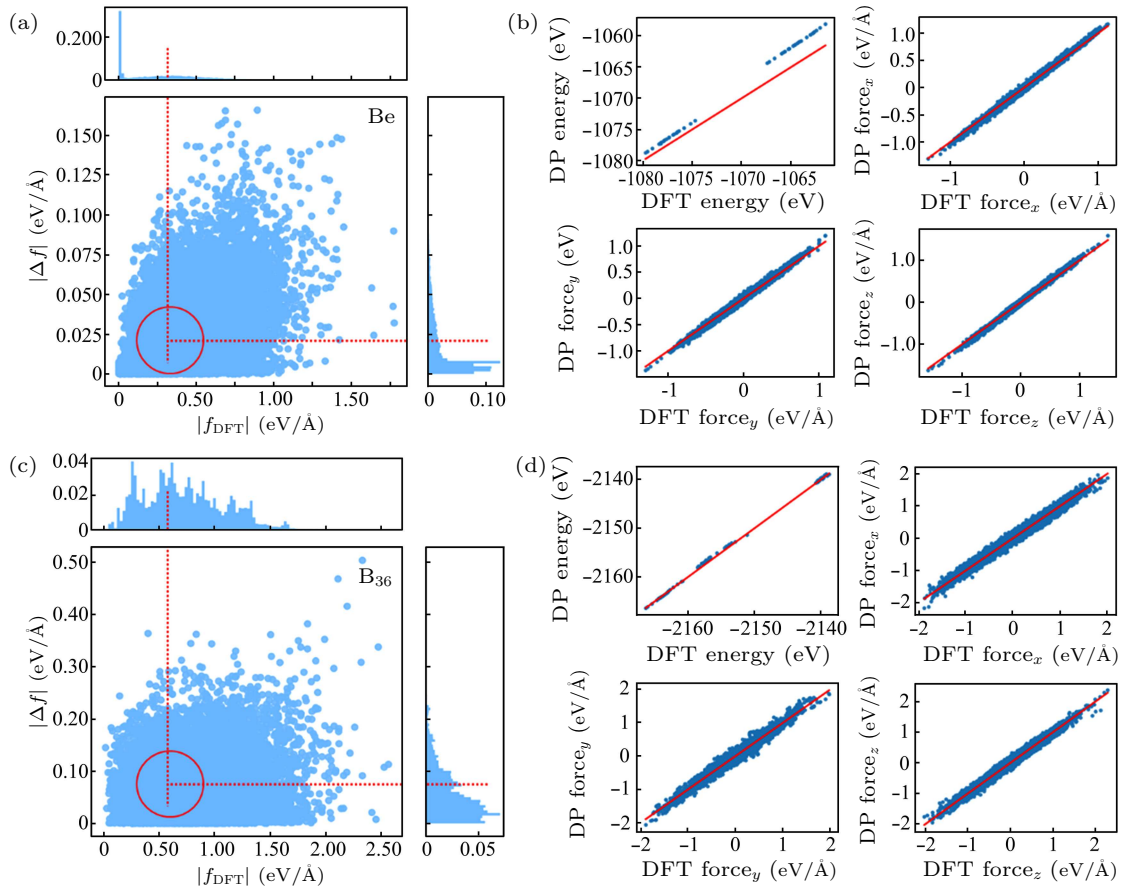


Fig. 3. The scatter histograms of force errors for the elements Be and B along with the data prediction fitting curves. (a) Scatter histograms for Be. (b) Data prediction fitting curves for Be. (c) Scatter histograms for B_{36}. (d) Data prediction fitting curves for B_{36}.

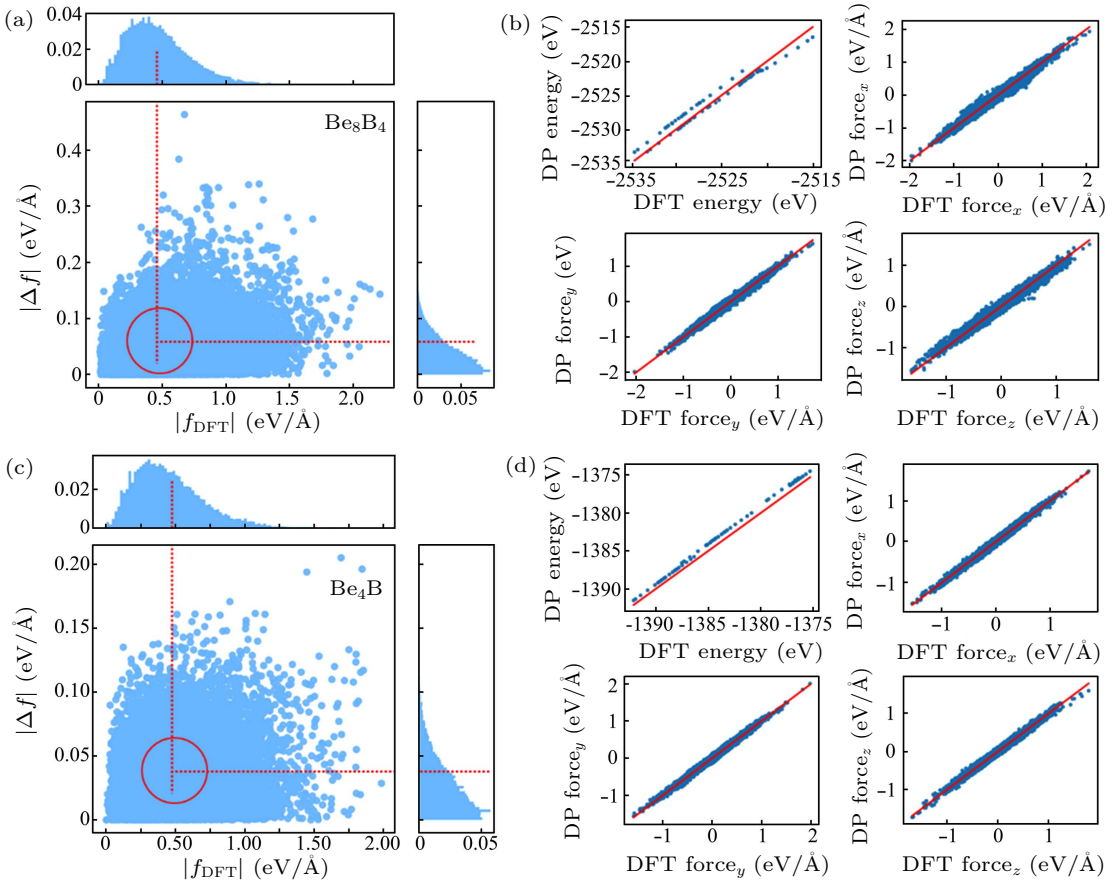


Fig. 4. The scatter histograms of force errors for BeB compounds along with the data prediction fitting curves. (a) Scatter histograms for Be_8B_4. (b) Data prediction fitting curves for Be_8B_4. (c) Scatter histograms for Be_4B. (d) Data prediction fitting curves for Be_4B.

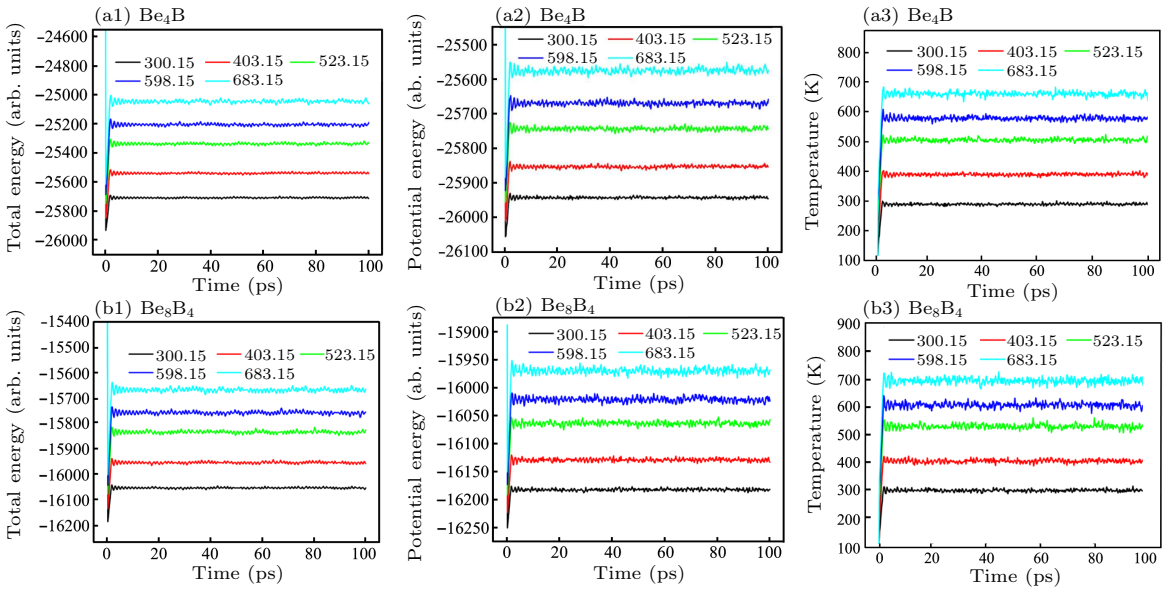


Fig. 5. The total energy, potential energy and temperature variation curves for Be_4B and Be_8B_4 during relaxation in the NPT ensemble: (a1) total energy of Be_4B, (b1) total energy of Be_8B_4, (a2) potential energy of Be_4B, (b2) potential energy of Be_8B_4, (a3) temperature of Be_4B, (b3) temperature of Be_8B_4.

Table 1. Comparison of elastic properties obtained from DP and DFT calculations for B_{36} (R-3m), Be_2 ($P6_3/mmc$), Be_4B ($P4/nmm$), and Be_8B_4 ($C2/m$).

	B_{36} R-3m		Be_2 $P63$-mmc		Be_4B $P4/nmm$		Be_8B_4 $C2/m$	
	This work	DFT	This work	DFT	This work	DFT	This work	DFT
Bulk modulus, Voigt (GPa)	210.41	212	125.08	120	150.69	138	160.24	145
Bulk modulus, Reuss (GPa)	208.87	208	124.67	120	150.17	138	151.11	145
Bulk modulus, Hill (GPa)	209.64	210	124.87	120	150.43	138	155.67	145

Then, we conducted NPT ensemble simulations on BeB crystals (Be_4B $P4/nmm$, Be_8B_4 $C2/m$) using the generated DP energy function to assess their stability. A 100 ps relaxation simulation was implemented. The analyses of variations in total energy, potential energy and temperature are presented in Fig. 5. This figure clearly demonstrates that the total energy, potential energy and temperature of the BeB crystals remain highly stable during the evolution of all simulated temperatures, indicating that the BeB crystals exist stably by their DP energy function.

The elastic matrix of the BeB material was calculated to comprehensively assess its mechanical properties, with the corresponding results summarized in Table 1. Comparison of elastic properties obtained from DP and DFT calculations for B_{36} (R-3m), Be_2 ($P63/mmc$), Be_4B ($P4/nmm$), and Be_8B_4 ($C2/m$) was made. A comparison of the data reveals that the bulk modulus obtained from the DP model closely matches that from DFT calculations, indicating good consistency. These results suggest that our potential can reliably capture and describe the mechanical behavior of BeB materials.

To further verify the accuracy of the potential, we conducted a series of simulations on a Be substrate, growing films with B doping ratios ranging from 4% to 24%, increasing in 4% increments. The evolution of the crystal ratio with the number of deposited atoms across this range of doping levels (from 4% to 24%) is illustrated in Fig. 6, with an incident energy of 5.0 eV and a substrate temperature of 403.15 K. This figure demonstrates that when B doping exceeds 15%, the crystalline fraction decreases, which is consistent with previously observed experimental results.[12–14]

By the analysis in this section, we have verified that the total energy, potential energy and temperature of the BeB crystals obtained with the DP energy function show high stability. Moreover, the sampling calculation from the first-principles dataset has verified that the accuracy of DP energy function is high for different systems. Therefore, our DP energy function can capture and describe the interaction between Be and B accurately.

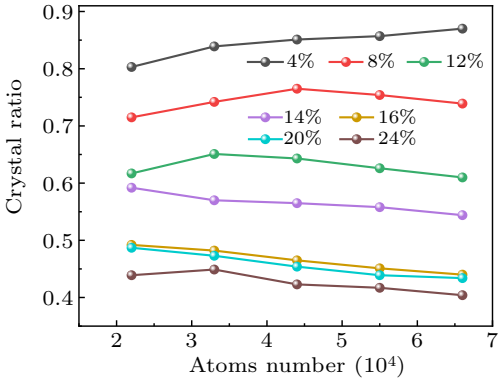


Fig. 6. Evolution of the crystal ratio with the number of deposited atoms, with an incident energy of 5.0 eV and a substrate temperature of 403.15 K.

3.2. The effect of incident energy on the film morphology

In magnetron sputtering experiments, when the target pellet is struck by high-energy ions the resulting clusters travel toward the substrate. The smaller clusters often have a higher momentum, making them more likely to reach the substrate surface. In contrast, the larger clusters may break apart during their journey, reducing their chances of arriving intact. As a result, the smaller clusters tend to predominate in the process. To better replicate these conditions and enhance the reliability of our results, we adopted a proportional deposition strategy. By controlling the sputtering frequency for different cluster sizes we aimed to closely mimic the actual sputtering process. During deposition, the incident frequencies for clusters of 3 Å, 5 Å, 7 Å and 9 Å were set at 60%, 25%, 10% and 5%, respectively. Existing experiments[13] have verified that when B doping increases to 15%, the crystalline columnar growth is significantly reduced and the grain size becomes notably finer. Therefore, our simulation focused on the Be–16 at.% B films. The substrate temperature was set at 403.15 K, with clusters impacting the substrate surface perpendicularly.

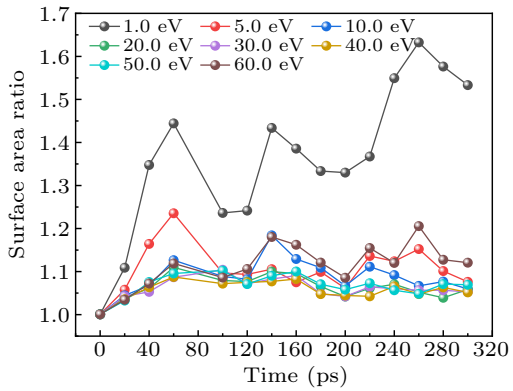


Fig. 7. The surface area ratio of films formed by clusters at different incident energies.

The relationship between incident energy and surface area is depicted in Fig. 7. It shows that when the clusters are deposited at a lower energy, such as 1.0 eV, the surface area ratio of the films is relatively larger, reaching 1.5 to 1.6 times the substrate area. This phenomenon is primarily due to the limited diffusion and migration ability of cluster atoms at a low energy, which causes them to adhere near the contact point with the substrate, resulting in island growth and increased surface roughness. With a moderate increase in incident energy, the downward impact force helps disperse the cluster atoms, allowing them to spread more evenly across the substrate and reducing local atomic aggregation, which smooths the surface of films. This effect is visually confirmed by images of the surface morphology of films deposited at various energies, shown in Fig. 7. However, an excessively high incident energy, such as above 30.0 eV, leads to an increase in the surface area ratio of the films. This is qualitatively observed in the surface morphology images illustrated in Fig. 8. This phenomenon occurs when secondary sputtering effects are triggered, disrupting the surface structure of the deposited films and leading to the formation of local pits and protrusions. Additionally, high-energy atoms may penetrate the surface or cause localized melting followed by rapid solidification, further increasing surface irregularities and resulting in roughening.

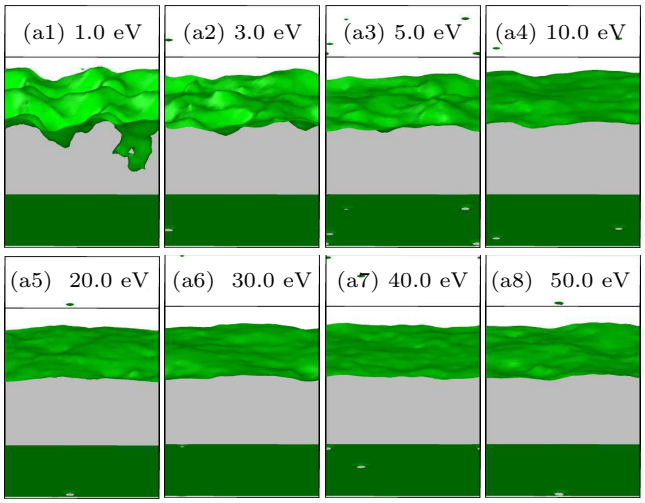


Fig. 8. The surface morphology of films at different incident energies, controlled from 1.0 eV to 50.0 eV.

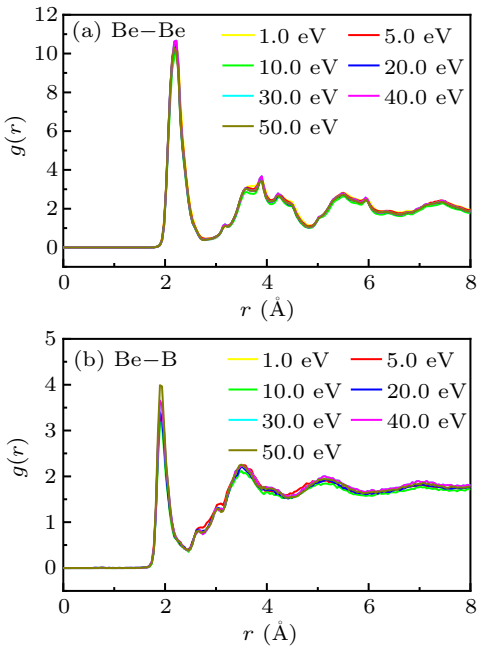


Fig. 9. The RDF of films formed by clusters at different incident energies, with the incident energy ranging from 1.0 eV to 50.0 eV: (a) Be–Be atomic pairs, (b) Be–B atomic pairs.

The RDF of films grown under different incident energies is represented in Fig. 9, with the incident energy ranging from 1.0 eV to 50.0 eV: (a) Be–Be atomic pairs, (b) Be–B atomic pairs. From the data, it is evident that while the RDF for Be–Be atomic pairs in the films shows little change, there are sub-

tle variations in the function for Be–B atomic pairs. For Be–B atomic pairs, the peak shape shows minimal change as the energy increases from 1 eV to 30 eV, with a slight increase in peak height, indicating enhanced local short-range order and improved local densification. However, as the energy rises to 50 eV the peak width broadens significantly, suggesting the emergence of greater local structural distortions. These phenomena are consistent with the analysis in Figs. 7 and 8.

These results indicate that a moderate increase in the incident energy can reduce the surface roughness of BeB films. Within the energy range of 10.0 eV/atom to 30.0 eV/atom the surface roughness remains low. This suggests that precise control of the incident energy can optimize the structural properties of the films, resulting in higher-quality deposition.

3.3. The effect of incident angle on the film morphology

In magnetron sputtering experiments, adjusting the incident angle of the particles offers a way to control the growth of films and tailor the final surface morphology for specific applications.[23] As analyzed in the previous section, we set the incident frequencies of the 3 Å, 5 Å, 7 Å and 9 Å clusters to 60%, 25%, 10% and 5%, respectively. To explore the impact of the incident angle on film growth, we simulated Be–16 at.% B films at a substrate temperature of 403.15 K, with incident energies of 5.0 eV/atom and 10.0 eV/atom. The incident angles were set to 0°, 15°, 30°, 45° and 60°.

Figure 10 shows how surface roughness evolves over deposition time. Figure 11 displays the final surface morphology of the deposited films. From these figures it is clear that at lower incident angles (below 30°) surface roughness is minimally affected by angle variations. However, once the incident angle exceeds 45°, the surface roughness rises sharply with increasing angle. This effect is possibly caused by the sputtered particles arriving at the substrate at higher tilt angles, distributing their kinetic energy primarily along the surface. Furthermore, it raises the possibility of atom reflection. This also causes micro-protrusions on the substrate to shade areas behind them, reducing the sputtered atom density in those regions. As time progresses, this uneven deposition causes the film to develop a rough, uneven surface.

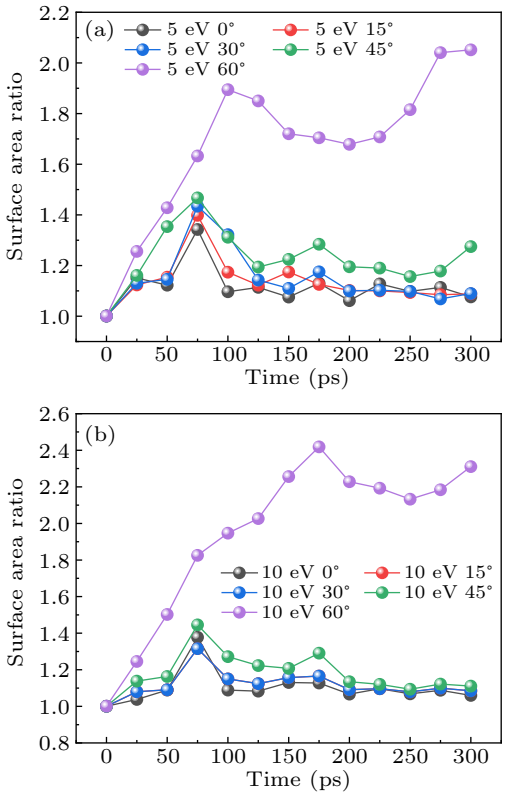


Fig. 10. The surface area ratio of films formed by clusters at different incident angles: (a) incident energy of 5.0 eV, (b) incident energy of 10.0 eV.

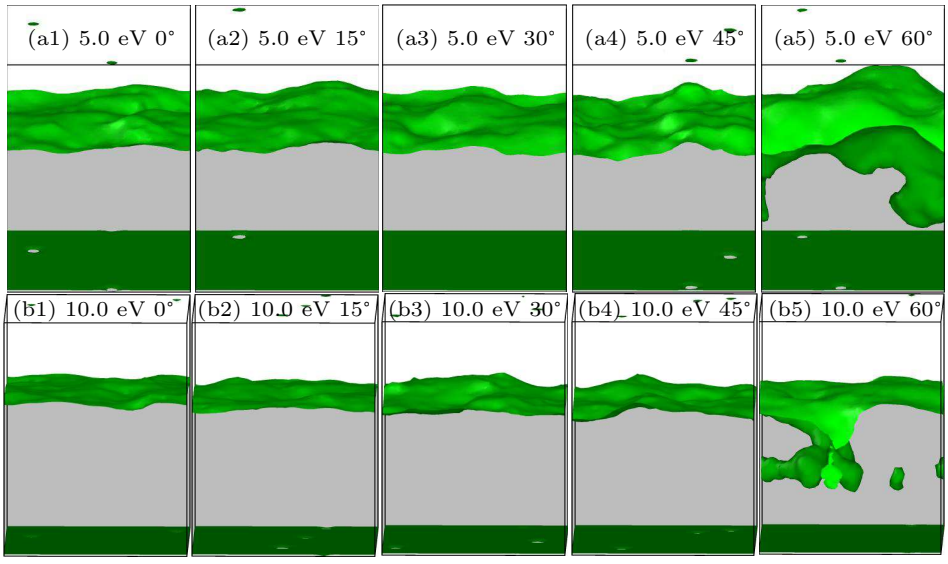


Fig. 11. The surface morphology of films formed at different incident angles with incident energies of 5.0 eV and 10.0 eV. The incident angle is controlled from 0° to 60° relative to the z-axis, with increments of 15°.

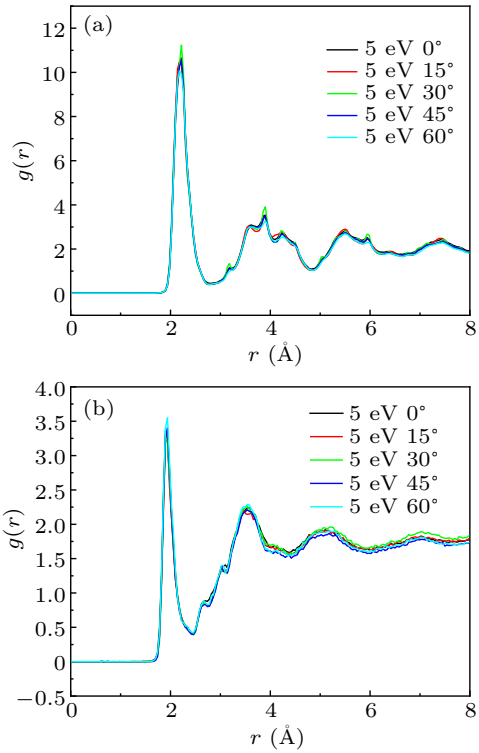


Fig. 12. The RDF of films formed by clusters at different incident angles with an incident energy of 5.0 eV: (a) Be–Be atomic pairs, (b) Be–B atomic pairs.

The RDF curves for Be–Be and Be–B atomic pairs at an incident energy of 5.0 eV at different incident angles are illustrated in Fig. 12. It is apparent that the peak height for Be–Be atomic pairs slightly decreases with increasing incidence angle, indicating a reduction in local short-range order. This suggests that at higher angles the atomic arrangement becomes less compact and more disordered, contributing to increased surface roughness. This observation aligns with our analysis for Figs. 10 and 11.

From the analyses above, we conclude that controlling the incident angle between 0° and 30° during sputter deposition can effectively maintain the surface roughness of films at a relatively low level.

3.4. The effect of substrate temperature on film morphology

In magnetron sputtering experiments, precise control of the substrate temperature can optimize the microstructure of films and reduce surface roughness.[24] In our study, we explored the effects of different substrate temperatures on Be–16 at.% B film under the same incident energy. Specifically, films grown at an incident energy of 1.0 eV/atom were subjected to heating treatments for 60 ps within the temperature range 273.15–1073.15 K.

Figures 13 and 14 show that as the temperature increases the roughness of the films initially decreases. This is because with a moderate rise in substrate temperature surface diffusion is enhanced, allowing atoms to migrate to lower-energy positions. However, as the temperature further increases (to 1073.15 K), the films become rougher. This is because excessive atomic migration, which may cause atoms to move away from their lowest-energy positions, disrupts surface uniformity. Additionally, high temperatures can lead to localized desorption or re-evaporation of atoms, and even induce thermal stress, all of which contribute to surface instability and increased roughness.

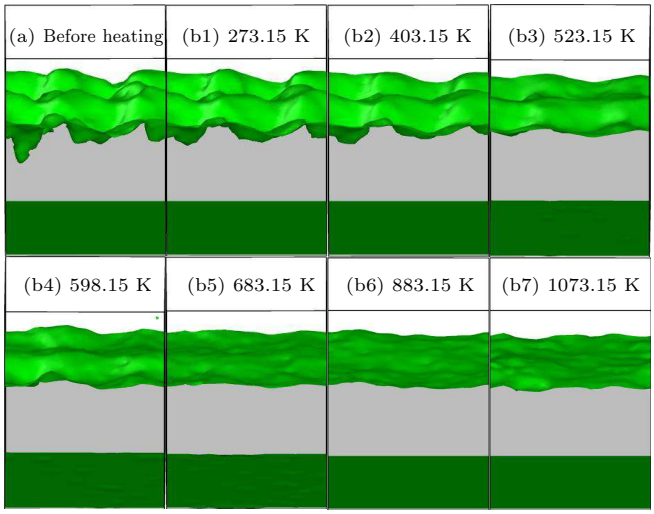


Fig. 13. The surface morphology of films formed at different substrate temperatures with incident energies of 1.0 eV: (a) surface morphology of the film before heating, (b1)–(b7) surface morphologies at different substrate temperatures.

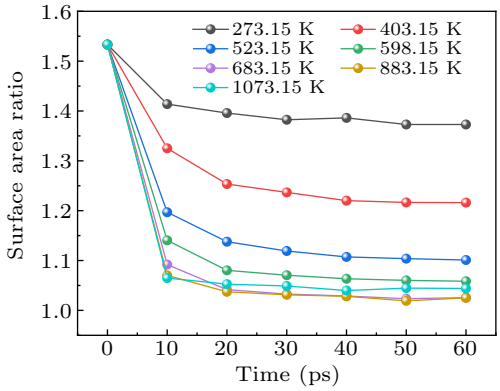


Fig. 14. The surface area ratio of films formed by clusters at different substrate temperatures.

We performed MSD analysis of the heating process at different temperatures. The results are shown in Fig. 15. It is evident that MSD exhibits a clear upward trend as the temperature increases, indicating that the diffusion and migration ability of atoms within the film is enhanced with increasing temperature. Specifically, when the temperature reaches 883.15 K, a sharp increase in MSD occurs. This is likely due to the rapid increase in atomic energy at high temperatures, enabling atoms to overcome local energy barriers and thereby enhancing their diffusion ability. However, when the temperature reaches 1073.15 K, MSD exhibits linear growth, indicating liquefaction of the film. All these findings are consistent with the surface morphology analysis in Fig. 13, further validating our conclusions.

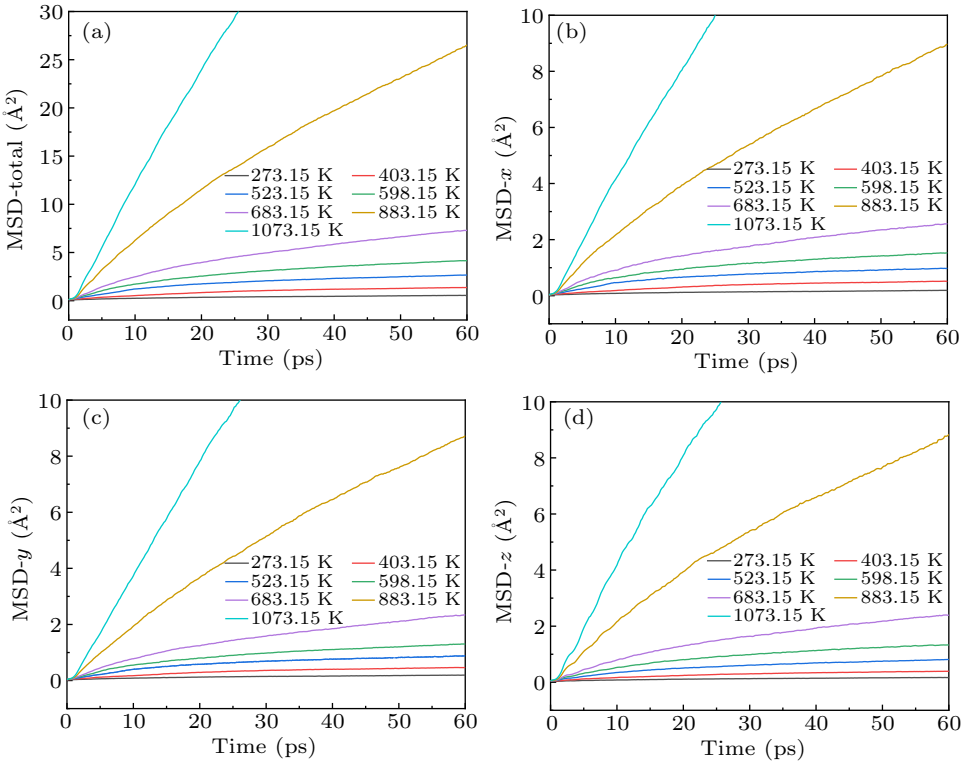


Fig. 15. The MSD of the films during the heating process with temperatures ranging from 273.15 K to 1073.15 K: (a) total MSD of the atoms, (b) MSD along the *x*-axis, (c) MSD along the *y*-axis, (d) MSD along the *z*-axis.

Furthermore, analysis of both the total MSD curve and the MSD curves along individual directions reveals that the diffusion ability of atoms in the film is roughly isotropic. Such isotropy is a key feature of typical amorphous materials, reflecting the absence of a distinct lattice arrangement and the presence of a uniform and disordered structure.

In this section, we have found that heating the films at a certain temperature can effectively reduce their roughness. However, when the temperature exceeds 883.15 K, localized liquefaction may occur, adversely affecting film growth quality. Therefore, we recommend heating the substrate to a temperature in the range of 683.15–883.15 K to achieve high-quality films.

4. Conclusions

In this study, we have developed a deep potential energy function which accurately describes Be–B interactions and provides a high-precision foundation for molecular dynamics simulations of the growth of BeB films, overcoming the limitations of existing methods. We explored the growth of BeB films formed by clusters. The results show that with increasing incident energy the surface area ratio of films decreases. However, when the incident energy exceeds 30.0 eV, the surface roughness of films begins to rise. Therefore, incident energies between 10.0 eV/atom and 30.0 eV/atom produce films with smoother surfaces. This suggests that precise control of the incident energy can optimize the structural properties of the films, resulting in a higher-quality deposition.

Keeping the incident angle between 0° and 30° yields a smoother film surface, while angles above 45° significantly increase the roughness. This suggests that adjusting the incident angle can effectively influence the surface morphology of the films.

Additionally, heating the films at a certain temperature (683.15–883.15 K) can effectively reduce their roughness. However, excessively high temperatures may cause the surface of the film to melt, thereby affecting its quality.

In short, our calculations demonstrate that by controlling the incident angle, energy and substrate temperature, high-quality BeB films can be achieved. We hope these findings will provide a solid theoretical foundation for experimental film fabrication, helping to enhance the controllability and efficiency of film preparation.

Acknowledgement

We acknowledge the support of the National Key R&D Program of China (Grant No. 2024YFF0508503).

References

[1] Lindl J D, Atherton L J, Amednt P A, *et al.* 2011 *Nucl. Fusion* **51** 094024
[2] Edwards M J, Lindl J D, Spears B K, *et al.* 2011 *Phys. Plasma* **18** 051003
[3] Zhang Z W, Qi X B and Li B 2012 *Acta Phys. Sin.* **61** 145204 (in Chinese)
[4] Puchta R 2011 *Nat. Chem.* **3** 416
[5] Haan S W, Pollaine S M, Lindl J D, *et al.* 1995 *Phys. Plasma* **2** 2480

[6] Yi S A, Simakov A N, Wilson D C, Olson R E, Kline J L, Clark D S, Hammel B A, Milovich J L, Salmonson J D, Kozioziemski B J and Batha S H 2014 *Phys. Plasma* **21** 092701

[7] Zylstra A B, Yi S A, MacLaren S, *et al.* 2018 *Phys. Plasma* **25** 102704

[8] Nikroo A, Xu H W, Moreno K A, Youngblood K P, Cooley J, Alford C S, Letts S A and Cook R C 2007 *Fusion Sci. Technol.* **51** 553

[9] Luo B, Zhang J, He Y, Chen L, Luo J, Li K and Wu W 2017 *High Power Laser Sci. Eng.* **5** e10

[10] McEachern R, Alford C, Cook R, Makowiecki D and Wallace R 1997 *Fusion Technol.* **31** 435

[11] Frost F, Fechner R, Ziberi B, Völlner J, Flamm D and Schindler A 2009 *J. Phys.: Condens. Matter* **21** 224026

[12] Jankowski A F, Wall M A, Van Buuren A W, Nieh T G and Wadsworth J 2002 *Acta Mater.* **50** 4791

[13] Li K, He Y, Luo J, Li W, Zhou M, Li B and Luo B 2021 *Fusion Eng. Des.* **172** 112727

[14] Xu H, Huang H, Walker J, Elsner F H and Farrell M P 2018 *Fusion Sci. Technol.* **73** 408

[15] Hardy H L 1980 *Environ. Res.* **21** 1

[16] Araghi H and Zabihi Z 2013 *Nucl. Instrum. Methods Phys. Res., Sect. B* **298** 13

[17] Guolong J and Xia Z 2024 *Chin. Phys. B* **33** 77901

[18] Sapra S and Sarma D D 2004 *Phys. Rev. B* **69** 125304

[19] Li J Y, Wu D, Li Y and Li Z R 2017 *Chem. Phys. Lett.* **674** 1

[20] Cerowski V, Rao B K, Khanna S N, Jena P, Ishii S, Ohno K and Kawazoe Y 2005 *J. Chem. Phys.* **123** 074329

[21] Kawai R and Weare J H 1990 *Phys. Rev. Lett.* **65** 80

[22] Cao Y, Zhang J, Wu C and Yu F 2013 *Thin Solid Films* **544** 496

[23] Hassani A, Makan A, Sbiaai K, Tabyaoui A and Hasnaoui A 2017 *Thin Solid Films* **640** 123

[24] Luo B C, Li K, Tan X L, Zhang J Q, Luo J S, Jiang X D, Wu W D and Tang Y J 2014 *J. Alloys Compd.* **607** 150

[25] Zhou X W, Johnson R A and Wadley H N G 1997 *Acta Mater.* **45** 1513

[26] Zhou X W, Wadley H N G, Johnson R A, Larson D J, Tabat N, Cerezo A, Petford-Long A K, Smith G D W, Clifton P H, Martens R L and Kelly T F 2001 *Acta Mater.* **49** 4005

[27] Zhou X W, Johnson R A and Wadley H N G 2004 *Phys. Rev. B* **69** 144113

[28] Mes-adi H, Herbazi R, Lablali M, Saadouni K and Mazroui M 2023 *Comput. Mater. Sci.* **222** 112117

[29] Byggmästar J, Hodille E A, Ferro Y and Nordlund K 2018 *J. Phys.: Condens. Matter* **30** 135001

[30] Brault P, Chamorro-Coral W, Chuon S, Caillard A, Bauchire J M, Baranton S, Coutanceau C and Neyts E 2019 *Front. Chem. Sci. Eng.* **13** 324

[31] Zhu G, Sun J, Zhang L and Gan Z 2018 *J. Cryst. Growth* **492** 60

[32] Sharkass M, Dwivedi S, Shin Y K, Nieto-Perez M, van Duin A C T and Krstic P S 2025 *J. Nucl. Mater.* **606** 155622

[33] Agrawal A, Mishra R, Ward L, Flores K M and Windl W 2013 *Modell. Simul. Mater. Sci. Eng.* **21** 085001

[34] Kang J W and Hwang H J 2004 *Comput. Mater. Sci.* **31** 237

[35] Bartók A P, Payne M C, Kondor R and Csányi G 2010 *Phys. Rev. Lett.* **104** 136403

[36] Zhang L, Han J, Wang H, Car R and E W 2018 *Phys. Rev. Lett.* **120** 143001

[37] Thompson A P, Swiler L P, Trott C R, Foiles S M and Tucker G J 2015 *J. Comput. Phys.* **285** 316

[38] Shapeev A V 2016 *Multiscale Modeling & Simulation* **14** 1153

[39] Behler J 2016 *J. Chem. Phys.* **145** 170901

[40] Konashi K, Kato N, Mori K and Kurosaki K 2025 *J. Nucl. Mater.* **607** 155660

[41] Kim J J, Kim E-S, Seong H W and Ryu H J 2025 *J. Nucl. Mater.* **605** 155532

[42] Liyanage M, Reith D, Eyert V and Curtin W A 2024 *J. Nucl. Mater.* **602** 155341

[43] Hirel P 2015 *Comput. Phys. Commun.* **197** 212

[44] Plimpton S 1995 *J. Comput. Phys.* **117** 1

[45] Brodtkorb A R, Hagen T R and Sætra M L 2013 *J. Parallel Distrib. Comput.* **73** 4

[46] Stukowski A 2010 *Modell. Simul. Mater. Sci. Eng.* **18** 015012

[47] Svishchev I M and Kusalik P G 1993 *J. Chem. Phys.* **99** 3049

[48] Chubynsky M V and Slater G W 2014 *Phys. Rev. Lett.* **113** 098302